Frontiers of Information Technology & Electronic Engineering
www.zju.edu.cn/jzus; engineering.cae.cn; www.springerlink.com
ISSN 2095-9184 (print); ISSN 2095-9230 (online)
E-mail: jzus@zju.edu.cn

Analysis and design of pulse frequency modulation dielectric barrier discharge for low power applications*

Tang-tang GUO†, Xing-liang LIU, Shi-qiang HAO, Chi ZHANG, Xiang-ning HE†‡

(*School of Electrical Engineering, Zhejiang University, Hangzhou 310027, China*)

†E-mail: gtt1024@gmail.com; hxn@zju.edu.cn

Received May 16, 2014; Revision accepted Aug. 8, 2014; Crosschecked Jan. 28, 2015

Abstract: For low power dielectric barrier discharge (DBD) used in small-size material treatment or portable devices, high-step transformer parasitic capacitance greatly influences the performance of the resonant converter as it is of the same order of magnitude as the equivalent capacitance of DBD load. In this paper, steady-state analysis of the low power DBD is presented, considering the inevitable parasitic capacitance of the high-step transformer. The rectifier-compensated first harmonic approximation (RCFHA) is applied to linearize the equivalent load circuit of DBD at low frequency and the derived expressions are accurate and convenient for the analysis and design of the power supply. Based on the proposed linear equivalent load circuit, the influence of transformer parasitic capacitance on the key parameters, including the frequency range and the applied electrode voltage, is discussed when the power is regulated with pulse frequency modulation (PFM). Also, a design procedure is presented based on the derived expressions. A prototype is constructed according to the design results and the accuracy of the design is verified by experimental results.

Key words: Dielectric barrier discharge, Rectifier-compensated first harmonic approximation, Parasitic capacitance, Power converter design

doi:10.1631/FITEE.1400185 **Document code:** A **CLC number:** TM46

1 Introduction

Dielectric barrier discharge (DBD) has been widely used in material treatment, ozone generation, biomedicine, etc. The plasma or ozone generated during discharge can be used for material surface characteristic modification, sterilization, and chemical vapor deposition (Fang *et al*., 2006; Wang and He, 2006; Burany *et al*., 2008; Wedaa *et al*., 2011; Kostov *et al*., 2013).

Usually, an AC high voltage is applied to the load as shown in Fig. 1a to generate discharge for industrial applications due to easy power regulation methods, simple topology, and high reliability. When the applied voltage is high enough, the air between the dielectric and the high voltage electrode breaks down and a corona discharge is initiated. As the voltage across the air gap is almost constant when a corona discharge occurs (Alonso *et al*., 2003), the equivalent circuit of the DBD load is as illustrated in Fig. 1a, where C_{g_s} represents the equivalent capacitance of the air gap, and C_{d_s} represents the equivalent capacitance of the dielectric (Wagner *et al*., 2003; Williamson *et al*., 2006; Bonaldo and Pomilio, 2010). The diode bridge circuit models the bidirectional voltage clamping properties of the constant corona discharge voltage. To produce the required AC high voltage, the resonant converter is usually applied, as well as a high-frequency high-step transformer which leads to galvanic isolation.

In high power DBD applications, the parasitic capacitance of the transformer is much smaller than

‡ Corresponding author
* Project supported by the National Natural Science Foundation of China (No. 51107115) and the China Postdoctoral Science Foundation (No. 20110491766)
ORCID: Tang-tang GUO, http://orcid.org/0000-0002-9603-0997

the equivalent capacitance of DBD load and thus negligible. Therefore, an inductor-capacitor-capacitor (LCC) series-parallel resonant converter is used as the equivalent circuit, which has been discussed in many papers (Gilbert *et al.*, 2007; Fu *et al.*, 2008; Martin-Ramos *et al.*, 2008). However, in low power applications, such as small-size material treatment or the portable medical device, the equivalent capacitance of DBD load and the transformer parasitic capacitance are of the same order of magnitude. Thus, parasitic capacitance must be taken into consideration and the conventional LCC resonant converter is no more suitable for analysis. The influence of parasitic capacitance should be discussed. Moreover, for higher portability and lower cost, the resonant inductor is integrated into the transformer by applying a magnetic integration technique (Fu *et al.*, 2008). Therefore, only one magnetic component is required (Fig. 1b).

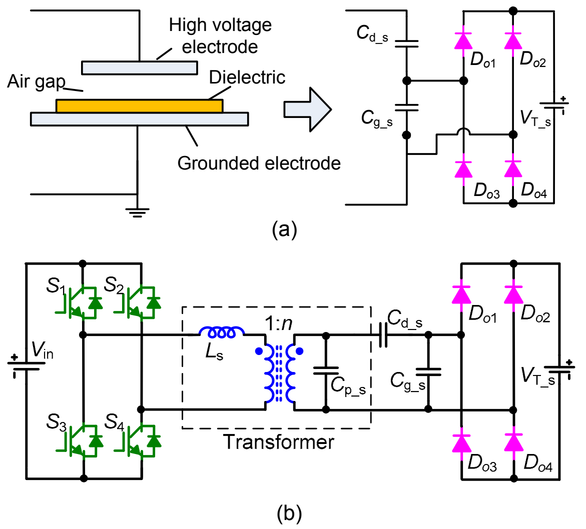

Fig. 1 Equivalent circuits of DBD load (a) and the whole resonant converter (b)

The notations used in this paper are given in Table 1.

To simplify the analysis, a capacitance in parallel with a resistance (RC) is used as the equivalent circuit of DBD load based on first harmonic approximation (FHA) (Alonso *et al.*, 2003; Kinnares and Hothongkham, 2010). However, FHA is not accurate enough for steady-state analysis due to the diode bridge circuit. Therefore, rectifier-compensated first harmonic approximation (RCFHA) (Shafiei *et al.*, 2013) is used for the steady-state analysis of the resonant converter with a rectified bridge. According to the equivalent circuit derived, the impact of

Table 1 The notations used in this paper

Parameter	Meaning
C_d	Dielectric equivalent capacitance referred to the primary side of the transformer
C_g	Air gap equivalent capacitance referred to the primary side of the transformer
V_T	Discharge maintaining voltage referred to the primary side of the transformer
L_s	Leakage inductance of the transformer
C_p	Transformer parasitic capacitance referred to the primary side of the transformer
n	Transformer turns ratio
f_s	Operating frequency
ω_s	Operating angular frequency, $\omega_s=2\pi f_s$
f_0	Resonant frequency
V_{in}	Bus voltage applied to the inverter
v_{ab}	Output voltage of the inverter
v_{ae}	Voltage applied to electrodes
V_{ae}	Peak value of v_{ae}
G_r	Resonant tank gain, $G_r=V_{ae}/(nV_{in})$
v_{cd}	Voltage applied to C_d
i_{cd}	Current flowing through C_d
v_{cg}	Voltage applied to C_g
i_r	Resonant current referred to the primary side of the transformer
I_r	Peak value of i_r
P_{in}	Average input power
P_{out}	Average output power
k_s	Load equivalent capacitance ratio, $k_s=C_d/C_g$
k_p	$k_p=C_p/C_d$
ψ	The angle of charging C_g
φ	Phase error between the output voltage of the inverter and resonant current
t_{db}	Dead band time
t_d	Time delay between the rising edge of driving signals and the corresponding zero-crossing point of the resonant current
t_{pe}	Time delay between the rising edge of the full-bridge output voltage and the resonant current
X_{y_norm}	Normalized variable X_y
X_{y_s}	Variable X_y referred to the secondary side of the transformer
X_{y1}	Fundamental harmonic component of X_y
X_{yA}	Coefficient of the Fourier sinusoidal term of X_{y1} at f_s
X_{yB}	Coefficient of the Fourier cosinusoidal term of X_{y1} at f_s

transformer parasitic capacitance on the frequency range and applied electrode voltage is discussed when the power is regulated with pulse frequency modulation (PFM), considering the different equivalent load parameters with varied output power (Wang *et al*., 2005). Then the design procedure is presented with the magnetic integration technique and the leakage inductance and parasitic capacitance of the transformer are given according to the results of steady-state analysis. The analysis and design are finally verified by simulation and experimental results.

2 Converter analysis

2.1 Steady-state analysis

A capacitor in series with a resistor is used to model C_g and the rectifier in RCFHA. Thus, the analysis is more accurate than that in FHA, where a resistor is used for equivalence. To simplify the analysis, all the parameters are referred to the primary side of the transformer (Fig. 2a).

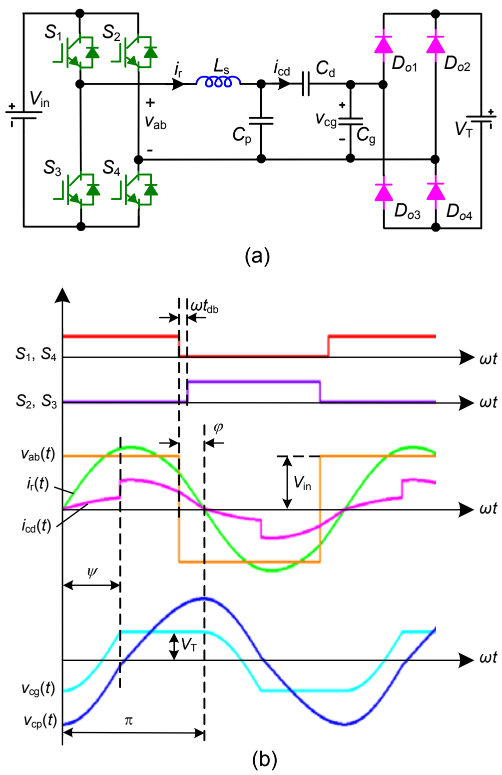

Fig. 2 Equivalent circuit of low power DBD referred to the primary side (a) and the key waveforms (b)

The key waveforms of the resonant converter are shown in Fig. 2b. As $i_r(t)$ is almost sinusoidal, it is assumed to be equal to its first harmonic component. That is,

$$i_{r1}(t)=i_r(t)=I_r\sin(\omega_s t). \tag{1}$$

According to whether C_g is clamped or not, the circuit operation can be divided into four stages. In the first half cycle, when $i_r(t)$ increases from zero, C_g is charged from $-V_T$ and the equivalent circuit is as shown in Fig. 3a. Thus, the following equations can be obtained:

$$i_{cd}(t)=\frac{1}{1+k_p+k_pk_s}I_r\sin(\omega_s t), \tag{2}$$

$$v_{cg}(t)=-V_T+\frac{I_r}{\omega_s C_g(1+k_p+k_pk_s)}(1-\cos(\omega_s t)). \tag{3}$$

At the end of this stage, $v_{cg}(t)$ increases to V_T. That is,

$$v_{cg}\left(\frac{\psi}{\omega_s}\right)=V_T. \tag{4}$$

By substituting Eq. (4) into Eq. (3), the following equation can be derived:

$$\cos\psi=1-\frac{2V_T\omega_s C_g(1+k_p+k_pk_s)}{I_r}. \tag{5}$$

Then C_g is charging to V_T and is clamped until $i_r(t)$ oscillates to zero. Thus, the equivalent circuit turns into the circuit shown in Fig. 3b. During this stage, $i_{cd}(t)$ and $v_{cg}(t)$ are given by

$$i_{cd}(t)=\frac{1}{1+k_p}I_r\sin(\omega_s t), \tag{6}$$

$$v_{cg}(t)=V_T. \tag{7}$$

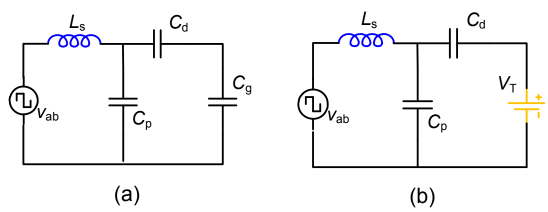

Fig. 3 Equivalent circuits when C_g is charging (a) and clamped (b)

The power transfers to the load during this stage. So, the output power can be obtained by integrating $v_{cg}(t)$ and $i_{cd}(t)$:

$$P_{\mathrm{out}}=\frac{V_{\mathrm{T}}I_{\mathrm{r}}(1+\cos\psi)}{\pi}\frac{1}{1+k_{\mathrm{p}}}. \tag{8}$$

Due to symmetry, $i_{cd}(t)$ and $v_{cg}(t)$ in one period can be summarized to be

$$i_{\mathrm{cd}}(t)=\begin{cases}\dfrac{1}{1+k_{\mathrm{p}}+k_{\mathrm{p}}k_{\mathrm{s}}}I_{\mathrm{r}}\sin(\omega_{\mathrm{s}}t), \\ \qquad 0\le t<\dfrac{\psi}{\omega_{\mathrm{s}}}\ \text{or}\ \pi\le t<\dfrac{\pi+\psi}{\omega_{\mathrm{s}}}, \\ \dfrac{1}{1+k_{\mathrm{p}}}I_{\mathrm{r}}\sin(\omega_{\mathrm{s}}t), \\ \qquad \dfrac{\psi}{\omega_{\mathrm{s}}}\le t<\pi\ \text{or}\ \dfrac{\pi+\psi}{\omega_{\mathrm{s}}}\le t<2\pi,\end{cases} \tag{9}$$

$$v_{\mathrm{cg}}(t)=\begin{cases}-V_{\mathrm{T}}+\dfrac{I_{\mathrm{r}}}{\omega_{\mathrm{s}}C_{\mathrm{g}}(1+k_{\mathrm{p}}+k_{\mathrm{p}}k_{\mathrm{s}})}(1-\cos(\omega_{\mathrm{s}}t)), \\ \qquad 0\le t<\psi/\omega_{\mathrm{s}}, \\ V_{\mathrm{T}}, \qquad \psi/\omega_{\mathrm{s}}\le t<\pi, \\ V_{\mathrm{T}}-\dfrac{I_{\mathrm{r}}}{\omega_{\mathrm{s}}C_{\mathrm{g}}(1+k_{\mathrm{p}}+k_{\mathrm{p}}k_{\mathrm{s}})}(1+\cos(\omega_{\mathrm{s}}t)), \\ \qquad \pi\le t<\dfrac{\pi+\psi}{\omega_{\mathrm{s}}}, \\ -V_{\mathrm{T}}, \qquad \dfrac{\pi+\psi}{\omega_{\mathrm{s}}}\le t<2\pi.\end{cases} \tag{10}$$

Using the Fourier analysis, the coefficients of the Fourier series of $i_{cd}(t)$ and $v_{cg}(t)$ are obtained as

$$I_{\mathrm{cdA}}=\frac{I_{\mathrm{r}}}{2\pi(1+k_{\mathrm{p}})(1+k_{\mathrm{p}}+k_{\mathrm{p}}k_{\mathrm{s}})}\cdot[(\sin(2\psi)+2\pi-2\psi)k_{\mathrm{p}}k_{\mathrm{s}}+2\pi(1+k_{\mathrm{p}})], \tag{11}$$

$$I_{\mathrm{cdB}}=\frac{-I_{\mathrm{r}}k_{\mathrm{p}}k_{\mathrm{s}}\sin^2\psi}{\pi(1+k_{\mathrm{p}})(1+k_{\mathrm{p}}+k_{\mathrm{p}}k_{\mathrm{s}})}, \tag{12}$$

$$V_{\mathrm{cgA}}=\frac{I_{\mathrm{r}}\sin^2\psi}{\pi C_{\mathrm{g}}\omega_{\mathrm{s}}(1+k_{\mathrm{p}}+k_{\mathrm{p}}k_{\mathrm{s}})}, \tag{13}$$

$$V_{\mathrm{cgB}}=\frac{-I_{\mathrm{r}}}{2\pi C_{\mathrm{g}}\omega_{\mathrm{s}}(1+k_{\mathrm{p}}+k_{\mathrm{p}}k_{\mathrm{s}})}(2\psi-\sin(2\psi)). \tag{14}$$

Thus, the equivalent impedance can be derived:

$$Z_{\mathrm{eq}}=\frac{V_{\mathrm{cgA}}+\mathrm{j}V_{\mathrm{cgB}}}{I_{\mathrm{cdA}}+\mathrm{j}I_{\mathrm{cdB}}}=R_{\mathrm{eq}}+\mathrm{j}X_{\mathrm{eq}}, \tag{15}$$

where R_{eq} and X_{eq} are given in Eqs. (16) and (17), respectively:

$$\begin{aligned}R_{\mathrm{eq}}=&\ \pi(1+k_{\mathrm{p}})(1+k_{\mathrm{p}}+k_{\mathrm{p}}k_{\mathrm{s}})\sin^2\psi\\ &\cdot\{C_{\mathrm{g}}\omega_{\mathrm{s}}\{(k_{\mathrm{p}}k_{\mathrm{s}}\sin^2\psi)^2+[\pi(1+k_{\mathrm{p}}+k_{\mathrm{p}}k_{\mathrm{s}})\\ &-k_{\mathrm{p}}k_{\mathrm{s}}(\psi-\sin\psi\cos\psi)]^2\}\}^{-1},\end{aligned} \tag{16}$$

$$\begin{aligned}X_{\mathrm{eq}}=&-(1+k_{\mathrm{p}})\{\pi(1+k_{\mathrm{p}}+k_{\mathrm{p}}k_{\mathrm{s}})(\psi-\sin\psi\cos\psi)\\ &-[(\psi-\sin\psi\cos\psi)^2+\sin^4\psi]k_{\mathrm{p}}k_{\mathrm{s}}\}\\ &\cdot\{C_{\mathrm{g}}\omega_{\mathrm{s}}\{(k_{\mathrm{p}}k_{\mathrm{s}}\sin^2\psi)^2+[\pi(1+k_{\mathrm{p}}+k_{\mathrm{p}}k_{\mathrm{s}})\\ &-k_{\mathrm{p}}k_{\mathrm{s}}(\psi-\sin\psi\cos\psi)]^2\}\}^{-1},\end{aligned} \tag{17}$$

Consequently, the equivalent circuit of RCFHA is obtained (Fig. 4a), where $C_{eq}=-1/(\omega_s X_{eq})$. By combining C_d and C_{eq}, the circuit can be simplified further (Fig. 4b), where $C_e=C_dC_{eq}/(C_d+C_{eq})$. Thus, the resonant converter shown in Fig. 1b is greatly simplified and the input impedance is derived as follows:

$$Z_{\mathrm{in}}=R_{\mathrm{in}}+\mathrm{j}X_{\mathrm{in}}, \tag{18}$$

where

$$R_{\mathrm{in}}=\frac{R_{\mathrm{eq}}C_{\mathrm{e}}^{2}}{(C_{\mathrm{p}}+C_{\mathrm{e}})^2+(\omega_{\mathrm{s}}C_{\mathrm{e}}C_{\mathrm{p}}R_{\mathrm{eq}})^2}, \tag{19}$$

$$X_{\mathrm{in}}=\omega_{\mathrm{s}}L_{\mathrm{s}}-\frac{C_{\mathrm{p}}+C_{\mathrm{e}}+C_{\mathrm{p}}\omega_{\mathrm{s}}^2C_{\mathrm{e}}^2R_{\mathrm{eq}}^2}{\omega_{\mathrm{s}}(C_{\mathrm{p}}+C_{\mathrm{e}})^2+\omega_{\mathrm{s}}^3C_{\mathrm{p}}^2C_{\mathrm{e}}^2R_{\mathrm{eq}}^2}. \tag{20}$$

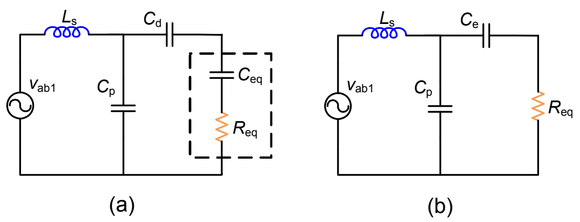

Fig. 4 Equivalent circuit of Fig. 2a in a steady condition (a) and the simplified circuit (b)

The phase error between the output voltage of the inverter and the resonant current, the peak resonant current and the peak applied electrode voltage are given in Eqs. (21)–(23), corresponding to the equivalent circuit in Fig. 4b:

$$\tan\varphi = X_{\text{in}} / R_{\text{in}}, \tag{21}$$

$$I_{\text{r}} = \frac{4V_{\text{ab}}}{\pi\sqrt{R_{\text{in}}^2 + X_{\text{in}}^2}}, \tag{22}$$

$$V_{\text{ae}} = I_{\text{r}}\sqrt{R_{\text{in}}^2 + X_{\text{in}}^2}. \tag{23}$$

The key parameters of the converter, including the peak applied electrode voltage, peak resonant current, resonant frequency, and quality factor, can be obtained from Eqs. (16)–(23). Therefore, the equivalent circuit shown in Fig. 4b can be used to describe the performance of low power DBD for simplicity.

2.2 Performance analysis

PFM is usually used to regulate the output power due to the simple control strategy and zero-voltage switch (ZVS) (Liu and He, 2005). The output power decreases with an increased operating frequency and ZVS is achieved for the whole power range. A narrow range of operating frequencies is preferred for the resonant converter from light load to full load, as the breakdown voltage of the transformer decreases significantly with increased frequency (Shafiei *et al.*, 2011).

On the other hand, the peak applied electrode voltage, which plays an important role in the number of microdischarges and surface treatment effect (Gibalov and Pietsch, 2000; Jidenko *et al.*, 2006), varies with the output power. In material treatment, the high applied electrode voltage may ruin or even burn the materials, while the low voltage may make the discharge unstable and result in uneven treatment. Consequently, it is necessary to investigate the influence of C_{p} on f_{s} and V_{ae}.

When the resonant tank operates at resonance, it is resistive and hence the resonant frequency can be derived from Eq. (20). Fig. 5 illustrates the operating frequency and tank gain at resonance with variant C_{p}. The resonant frequency increases with decreased C_{p}, which results in high power density. However, the tank gain of the resonant converter diminishes in the meantime and the voltage pressure of the switches increases when a constant V_{ae} is required for stable discharge. Hence, a tradeoff should be made if necessary.

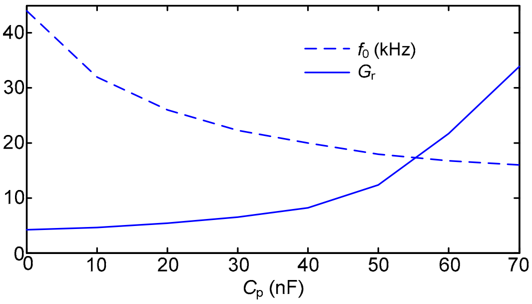

Fig. 5 Resonant frequency and tank gain with variant C_{p}

To simplify the analysis in PFM, the normalized results are used (Gilbert *et al.*, 2007). The normalized frequencies of the resonant converter from full load to light load with variant C_{p} are as illustrated in Fig. 6a, where C_{p}=0 represents that the converter is the conventional LCC resonant converter without parasitic capacitance. Fig. 6b shows the normalized peak applied electrode voltage. What is more, the equivalent capacitance of DBD load varies with the peak applied electrode voltage. C_{d} decreases from 48 nF to 32 nF with decreased V_{ae}, while C_{g} is assumed to be a constant of 16 nF, corresponding to the conclusions in Wang *et al.* (2005). The curves in Fig. 6a demonstrate that a larger C_{p} results in a narrower frequency range from full load to light load as C_{p} counteracts the influence of non-constant equivalent capacitance of DBD load, which simplifies the transformer design and improves the reliability. On the other hand, V_{ae} decreases faster in PFM with a larger C_{p}, which may influence the discharge stability and change the characteristics. Therefore, a compromise should be made when selecting C_{p} according to the requirements.

3 Design considerations

Based on the expressions derived in Section 2, the design procedure for a specified DBD load is presented as an example. The DBD load consists of two round planar electrodes and a 1 mm thick, flat piece of quartz as the dielectric as shown in Fig. 1a. The diameters of the high voltage electrode, quartz dielectric, and grounded electrode are 3, 5, and 6 cm, respectively. The parameters of the load in rated conditions are listed in Table 2. In a resonant converter with DBD load, the operating frequency is a little higher than the resonant frequency for ZVS as shown in Fig. 7. When switches S_1 and S_4 are turned on, the resonant current flows through the reverse parallel diodes and the voltage through the two switches is zero. Thus, ZVS is achieved and t_d is defined to be the time delay between the rising edge of the driving signals and the corresponding zero-crossing point of the current. By adding the dead band, t_{db}, to t_d, the total time the output voltage of the inverter leading the resonant current, t_{pe}, is obtained. In this study, t_{db} and t_{pe} are specified to be 2 μs and 4 μs in the rated condition, respectively.

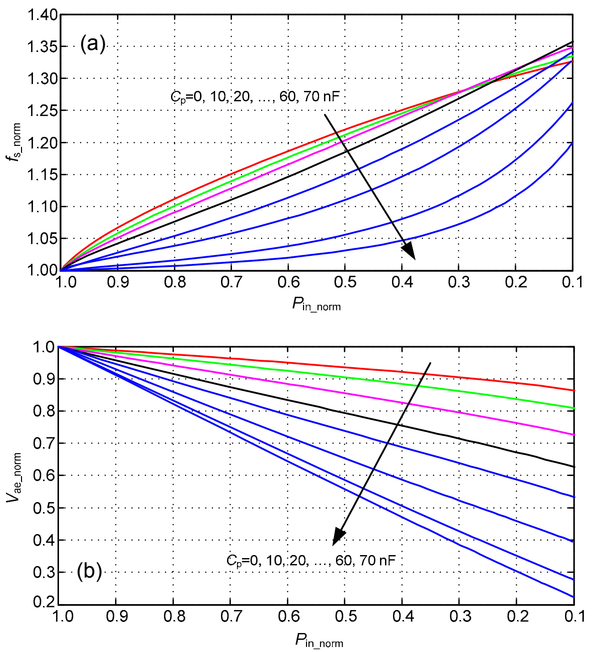

Fig. 6 Performance comparison of variant C_p in the normalized frequency (a) and the normalized applied electrode voltage with PFM (b)

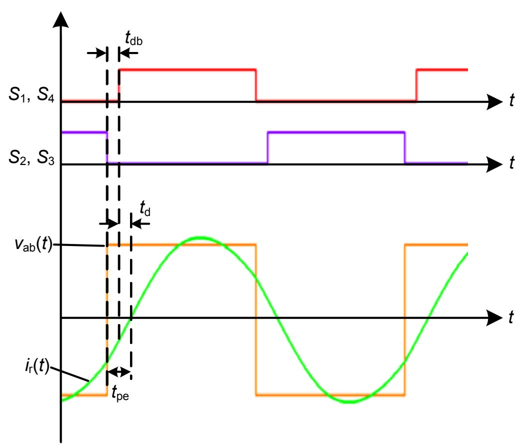

Fig. 7 Zero-voltage switch (ZVS) waveforms

Table 2 Converter specification

Parameter	Value
P_{in}	26 W
C_d	30 pF
C_g	10 pF
V_T	2900 V
V_{ab}	24 V
f_s	20 kHz
t_{pe}	4 μs

As the magnetic integration technique is applied, n, L_s, and C_p are the only three parameters required to be determined. For explicit n and C_p, I_r and ψ can be deduced by combining Eqs. (5) and (8):

$$I_r = \frac{\pi P_{in}(1+k_p)}{2V_T} + V_T\omega_s C_g(1+k_p+k_p k_s), \tag{24}$$

$$\psi = \arccos\left(\frac{\pi P_{in}(1+k_p) - 2V_T^2\omega_s C_g(1+k_p+k_p k_s)}{\pi P_{in}(1+k_p) + 2V_T^2\omega_s C_g(1+k_p+k_p k_s)}\right). \tag{25}$$

Thus, R_{eq}, X_{eq}, and R_{in} are obtained, corresponding to Eqs. (16), (17), and (19), respectively. Then L_s can be derived by substituting Eqs. (19), (20), and (24) into Eq. (22):

$$L_s = \sqrt{\left(\frac{4V_{ab}}{\pi\omega_s I_r}\right)^2 - \left(\frac{R_{in}}{\omega_s}\right)^2} + \frac{C_p + C_e + C_p\omega_s^2 C_e^2 R_{eq}^2}{\omega_s^2 (C_p+C_e)^2 + \omega_s^4 C_p^2 C_e^2 R_{eq}^2}. \tag{26}$$

X_{in} is obtained by substituting Eq. (26) into Eq. (20). Then φ is calculated according to Eq. (21). And

$$t_{pe} = \frac{\varphi}{\omega_s}. \tag{27}$$

The 3D figure in Fig. 8a illustrates t_{pe} with variant n and C_p corresponding to Eq. (27) and the curves of L_s are given in Fig. 8b according to Eq. (26). The design procedure can be subdivided into the following steps based on the curves:

Step 1: Select n and C_p. The purple curve in Fig. 8a includes the points at which t_{pe} is 4 μs. Here n is selected to be 40 for convenient calculation, a low transformer turns ratio and hence a small C_p for

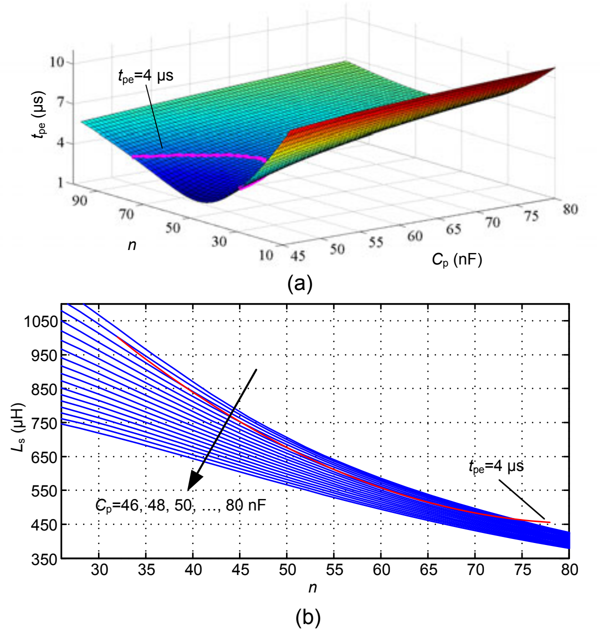

Fig. 8 Design curves at variant C_p and n: (a) t_{pe}; (b) L_s
References to color refer to the online version of this figure

the narrow applied electrode voltage range from full load to light load as presented in Section 2. Consequently, C_p is 52 nF.

Step 2: Calculate the transformer leakage inductance. The red curve in Fig. 8b represents the pairs of C_p and n at which t_{pe} is 4 μs. Thus, L_s is determined to be 827 μH corresponding to the parameters determined in Step 1.

Step 3: Calculate current stress. The peak resonant current is 1.94 A according to Eq. (24) for the specified n and C_p, which is helpful for selecting switches.

Step 4: Check the tolerance of C_p and L_s. C_p is highly affected by the structure of windings and the insulated materials used between the layers (Shafiei *et al*., 2011). Moreover, in high voltage applications, a core type transformer is usually used for its high insulating property, and the leakage inductance is difficult to calculate (Doebbelin *et al*., 2008). Thus, C_p and L_s cannot be designed exactly and the error tolerance should be taken into account. Table 3 lists the key parameters when C_p and L_s are changed by 10%. It shows that 10% errors of C_p and L_s bring approximately a 15% error in the rated power when t_{pe} is fixed to be 4 μs. However, a tiny change of the operating frequency, no more than 9%, guarantees the required rated power and ZVS is still achieved. Therefore, a minor error of C_p and L_s in the prototype is tolerable.

Table 3 The key parameters when C_p and L_s are changed by 10%

Parameter	Value				
	C_p=52 nF, L_s=827 μH	C_p=47 nF, L_s=744 μH		C_p=57 nF, L_s=910 μH	
		Fixed t_{pe}	Fixed P_{in}	Fixed t_{pe}	Fixed P_{in}
P_{in} (W)	26.0	23.0	26.2	29.8	26.5
I_r (A)	1.94	1.78	1.91	2.17	2.03
f_s (kHz)	20.0	22.3	21.8	18.1	18.4
t_{pe} (μs)	4.00	4.06	3.28	3.99	4.71

4 Simulation and experimental results

A prototype of the transformer shown in Fig. 9 is built corresponding to the parameters obtained in the design procedure, and the practical transformer parameters are listed in Table 4. The magnetic core comprises a pair of UF120A/70/30, which is Mn-Zn ferrite material.

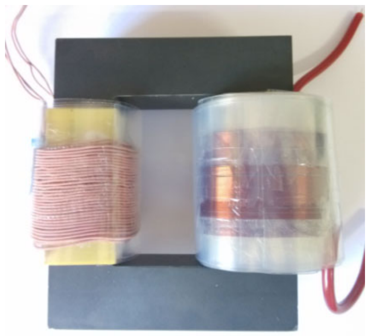

Fig. 9 Transformer prototype

Table 4 Transformer parameters

Parameter	Value	
	Design	Prototype
n	40	40
C_p	52 nF	49 nF
L_s	827 μH	880 μH

A low power DBD system with the built transformer is used to verify the equivalent circuit and design procedure. In practice, C_p is 54 nF in the calculation as the high voltage probe (P6015, Tektronix) results in an extra 3 pF capacitance referred to the secondary side (approximate 5 nF referred to the primary side of the transformer) in parallel with the load when measuring the applied electrode voltage. Fig. 10a illustrates the simulation waveforms corresponding to the prototype parameters while neglecting the parasitic capacitance, which differs greatly from the experimental waveforms in Fig. 10d. Consequently, C_p greatly influences the performance of DBD and should be carefully taken into consideration. In comparison with the experimental waveforms, the simulation waveforms from the converter with a rectified bridge as shown in Fig. 1b and the converter with an equivalent resonant model as shown in Fig. 4b are illustrated in Figs. 10b and 10c, respectively. There is a voltage drop when the current commutes from the diodes to the switches due to the switches' turn-on voltage and the diodes' forward voltage drop. Table 5 lists the key parameters of simulation, calculation with an equivalent model, and experiments, which confirm the steady-state analysis and design procedure a good accuracy.

The output power is regulated by PFM and t_{pe} is the control variable with self-sustained oscillation to maintain ZVS (Youssef and Jain, 2007; Gilbert *et al.*, 2008). Figs. 11a–11c show the experimental waveforms at variant frequencies, which illustrate that the input power of the resonant tank decreases with the increased frequency and that ZVS is achieved in the whole power range. When t_{pe} is larger than 10 μs, the applied electrode voltage is too low and the discharge in the air gap almost disappears. Table 6 gives the key parameters of the converter with an equivalent model, in comparison with the experimental results at variant frequencies, which verifies the accuracy of the equivalent resonant tank in steady-state conditions at different power levels.

Table 5 Simulation, calculation, and experimental results in rated conditions

Parameter	Value		
	Simulation with C_p	Calculation	Experiments
P_{in} (W)	26.6	27.3	26.8
I_r (A)	1.91	1.98	2.05
f_s (kHz)	19.0	19.0	18.1
t_{pe} (μs)	4.03	3.91	4.00
V_{ae} (kV)	7.86	8.03	7.76

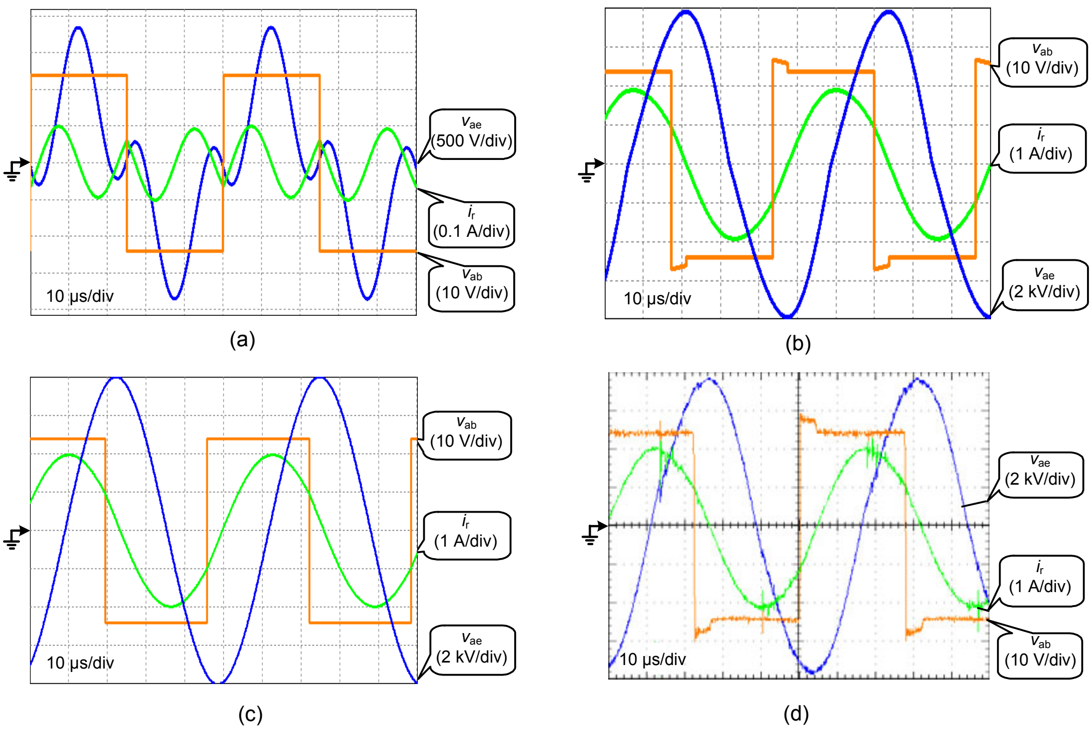

Fig. 10 Waveforms of i_r, v_{ab}, and v_{ae} in a rated condition in simulation without C_p (a), simulation from Fig. 1b (b), simulation with an equivalent model from Fig. 4b (c), and experiments (d)

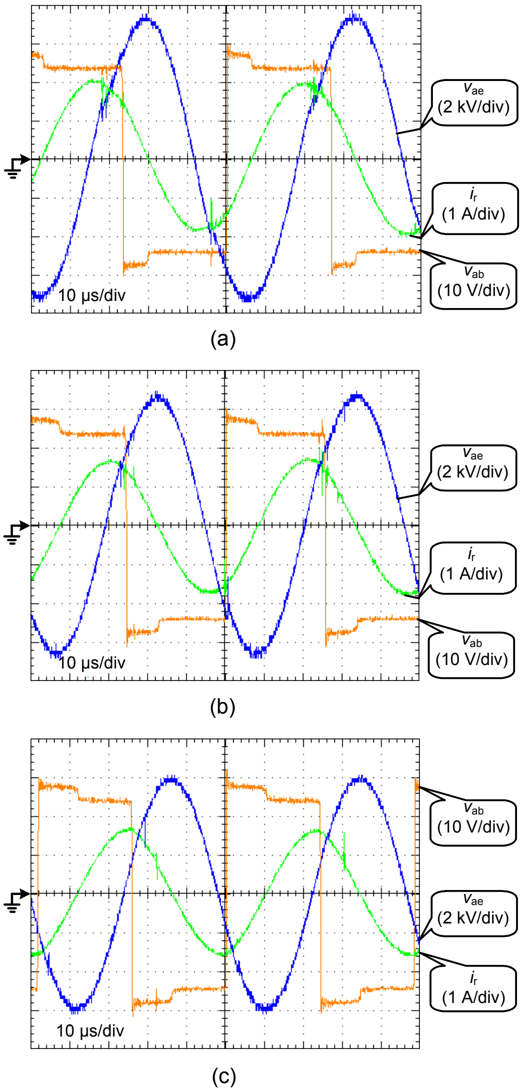

Fig. 11 Experimental waveforms when t_{pe}=6 μs (a), t_{pe}=8 μs (b), and t_{pe}=10 μs (c)

Table 6 Calculation and experimental results at variant frequencies

t_{pe} (μs)	P_{in} (W)		f_s (kHz)		I_r (A)		V_{ae} (kV)	
	Cal.	Exp.	Cal.	Exp.	Cal.	Exp.	Cal.	Exp.
6	23.3	23.0	19.6	18.7	1.92	1.95	7.75	7.80
8	15.4	15.3	20.7	19.6	1.81	1.75	7.36	6.80
10	4.59	4.53	21.8	20.7	1.57	1.65	6.17	6.00

Cal.: calculation result; Exp.: experimental result

As RCFHA is based on the sinusoidal resonant current, the accuracy of the equivalent model is greatly influenced by the total harmonic distortion (THD) of the resonant current. Fig. 12 illustrates the harmonic magnitude of the experimental resonant current as a percentage of the fundamental amplitude in the rated condition. Table 7 gives the THDs of the resonant current at variant frequencies derived from the simulation and experimental waveforms, which confirm that RCFHA is accurate in all steady-state conditions when power is regulated by the operating frequency. Therefore, the equivalent model is able to replace the original resonant converter with a rectified bridge for simpler performance analysis and design procedure.

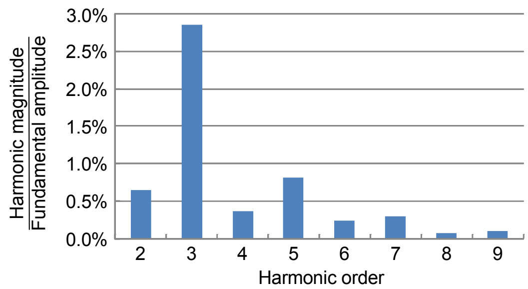

Fig. 12 Harmonic magnitude of experimental resonant current as a percentage of the fundamental amplitude in the rated condition

Table 7 The total harmonic distortion (THD) of resonant current at variant frequencies

f_s (kHz)	THD	
	Simulation	Experiment
18.1	3.16%	3.10%
18.7	2.29%	2.69%
19.6	1.40%	2.16%
20.7	2.62%	2.89%

5 Conclusions

The power supply with a high-step transformer for low power DBD was investigated, taking the parasitic capacitance of the transformer into consideration. RCFHA was used in steady-state analysis and the derivation was given in detail, corresponding to the equivalent circuit of DBD load. The parasitic capacitance greatly influences the converter performance in low power DBD applications and a compromise between the small frequency difference and the stable peak electrode voltage should be made when determining its value. The design procedure of the power supply was presented with the magnetic integration technique according to the expressions derived by an example. Finally, a prototype with two planar electrodes was built according to the design parameters and the experimental results were in good agreement with the design.

References

Alonso, J.M., Valdés, M., Calleja, A.J., *et al.*, 2003. High frequency testing and modeling of silent discharge ozone generators. *Ozone Sci. Eng.*, **25**(5):363-376. [doi:10.1080/01919510390481685]

Bonaldo, J.P., Pomilio, J.A., 2010. Control strategies for high frequency voltage source converter for ozone generation. Proc. IEEE Int. Symp. on Industrial Electronics, p.754-760. [doi:10.1109/ISIE.2010.5637402]

Burany, N., Huber, L., Pejovic, P., 2008. Corona discharge surface treater without high voltage transformer. *IEEE Trans. Power Electron.*, **23**(2):993-1002. [doi:10.1109/TPEL.2007.915760]

Doebbelin, R., Benecke, M., Lindemann, A., 2008. Calculation of leakage inductance of core-type transformers for power electronic circuits. Proc. 13th Power Electronics and Motion Control Conf., p.1280-1286. [doi:10.1109/EPEPEMC.2008.4635445]

Fang, Z., Qiu, X., Qiu, Y., *et al.*, 2006. Dielectric barrier discharge in atmospheric air for glass-surface treatment to enhance hydrophobicity. *IEEE Trans. Plasma Sci.*, **34**(4):1216-1222. [doi:10.1109/TPS.2006.877619]

Fu, D., Lee, F.C., Qiu, Y., *et al.*, 2008. A novel high-power-density three-level LCC resonant converter with constant-power-factor-control for charging applications. *IEEE Trans. Power Electron.*, **23**(5):2411-2420. [doi:10.1109/TPEL.2008.2002052]

Gibalov, V.I., Pietsch, G.J., 2000. The development of dielectric barrier discharges in gas gaps and on surfaces. *J. Phys. D Appl. Phys.*, **33**(20):2618-2636. [doi:10.1088/0022-3727/33/20/315]

Gilbert, A.J., Bingham, C.M., Stone, D.A., *et al.*, 2007. Normalized analysis and design of LCC resonant converters. *IEEE Trans. Power Electron.*, **22**(6):2386-2402. [doi:10.1109/TPEL.2007.909243]

Gilbert, A.J., Bingham, C.M., Stone, D.A., *et al.*, 2008. Self-oscillating control methods for the LCC current-output resonant converter. *IEEE Trans. Power Electron.*, **23**(4):1973-1986. [doi:10.1109/TPEL.2008.925198]

Jidenko, N., Petit, M., Borra, J.P., 2006. Electrical characterization of microdischarges produced by dielectric barrier discharge in dry air at atmospheric pressure. *J. Phys. D Appl. Phys.*, **39**(2):281-293. [doi:10.1088/0022-3727/39/2/008]

Kinnares, V., Hothongkham, P., 2010. Circuit analysis and modeling of a phase-shifted pulsewidth modulation full-bridge-inverter-fed ozone generator with constant applied electrode voltage. *IEEE Trans. Power Electron.*, **25**(7):1739-1752. [doi:10.1109/TPEL.2010.2042075]

Kostov, K.G., Nishime, T.M.C., Hein, L.R.O., *et al.*, 2013. Study of polypropylene surface modification by air dielectric barrier discharge operated at two different frequencies. *Surf. Coat. Technol.*, **234**:60-66. [doi:10.1016/j.surfcoat.2012.09.041]

Liu, Y., He, X., 2005. PDM and PFM hybrid control of a series-resonant inverter for corona surface treatment. *IEE Proc.-Electr. Power Appl.*, **152**(6):1445-1450. [doi:10.1049/ip-epa:20045270]

Martin-Ramos, J.A., Pernia, A.M., Diaz, J., *et al.*, 2008. Power supply for a high-voltage application. *IEEE Trans. Power Electron.*, **23**(4):1608-1619. [doi:10.1109/TPEL.2008.925153]

Shafiei, N., Pahlevaninezhad, M., Farzanehfard, H., *et al.*, 2011. Analysis and implementation of a fixed-frequency LCLC resonant converter with capacitive output filter. *IEEE Trans. Ind. Electron.*, **58**(10):4773-4782. [doi:10.1109/TIE.2011.2116758]

Shafiei, N., Pahlevaninezhad, M., Farzanehfard, H., *et al.*, 2013. Analysis of a fifth-order resonant converter for high-voltage DC power supplies. *IEEE Trans. Power Electron.*, **28**(1):85-100. [doi:10.1109/TPEL.2012.2200301]

Wagner, H.E., Brandenburg, R., Kozlov, K.V., *et al.*, 2003. The barrier discharge: basic properties and applications to surface treatment. *Vacuum*, **71**(3):417-436. [doi:10.1016/S0042-207X(02)00765-0]

Wang, C., He, X., 2006. Preparation of hydrophobic coating on glass surface by dielectric barrier discharge using a 16 kHz power supply. *Appl. Surf. Sci.*, **252**(23):8348-8351. [doi:10.1016/j.apsusc.2005.11.042]

Wang, H., Fang, Z., Qiu, Y., *et al.*, 2005. On the changing of equivalent capacitance in dielectric barrier discharge. *Insul. Mater.*, **38**(1):37-40. [doi:10.3969/j.issn.1009-9239.2005.01.012] (in Chinese).

Wedaa, H., Abdel-Salam, M., Ahmed, A., *et al.*, 2011. NO removal using dielectric barrier discharges in a multirod reactor stressed by AC and pulsed high voltages. *IEEE Trans. Dielectr. Electr. Insul.*, **18**(5):1743-1751. [doi:10.1109/TDEI.2011.6032846]

Williamson, J.M., Trump, D.D., Bletzinger, P., *et al.*, 2006. Comparison of high-voltage ac and pulsed operation of a surface dielectric barrier discharge. *J. Phys. D Appl. Phys.*, **39**(20):4400-4406. [doi:10.1088/0022-3727/39/20/016]

Youssef, M.Z., Jain, P.K., 2007. Series-parallel resonant converter in self-sustained oscillation mode with the high-frequency transformer-leakage-inductance effect: analysis, modeling, and design. *IEEE Trans. Ind. Electron.*, **54**(3):1329-1341. [doi:10.1109/TIE.2007.892742]